

Critical computational aspects of near infrared circular tomographic imaging: Analysis of measurement number, mesh resolution and reconstruction basis

Phaneendra K. Yalavarthy[§], Hamid Dehghani^{§,†}, Brian W. Pogue[§] and Keith D. Paulsen[§]

[§]Thayer School of Engineering, Dartmouth College, Hanover, New Hampshire 03755

[†]School of Physics, University of Exeter, Exeter, UK EX4 4QL

Phaneendra.K.Yalavarthy@dartmouth.edu, Brian.W.Pogue@dartmouth.edu

Abstract: The image resolution and contrast in Near-Infrared (NIR) tomographic image reconstruction are affected by parameters such as the number of boundary measurements, the mesh resolution in the forward calculation and the reconstruction basis. Increasing the number of measurements tends to make the sensitivity of the domain more uniform reducing the hypersensitivity at the boundary. Using singular-value decomposition (SVD) and reconstructed images, it is shown that the numbers of 16 or 24 fibers are sufficient for imaging the 2D circular domain for the case of 1% noise in the data. The number of useful singular values increases as the logarithm of the number of measurements. For this 2D reconstruction problem, given a computational limit of 10 sec per iteration, leads to choice of forward mesh with 1785 nodes and reconstruction basis of 30×30 elements. In a three-dimensional (3D) NIR imaging problem, using a single plane of data can provide useful images if the anomaly to be reconstructed is within the measurement plane. However, if the location of the anomaly is not known, 3D data collection strategies are very important. Further the quantitative accuracy of the reconstructed anomaly increased approximately from 15% to 89% as the anomaly is moved from the centre to boundary, respectively. The data supports the exclusion of out of plane measurements may be valid for 3D NIR imaging.

©2006 Optical Society of America

OCIS codes: (170.0170) Medical optics and biotechnology; (100.3190) Inverse problems; (170.3660) Light propagation in tissues; (170.4580) Optical diagnostics for medicine; (170.7050) Turbid media.

References and links

1. D. A. Boas, D. H. Brooks, E. L. Miller, C. A. DiMarzio, M. Kilmer, R. J. Gaudette, and Q. Zhang, "Imaging the body with diffuse optical tomography," *IEEE Signal Process. Mag.* **18**, 57-75 (2001).
2. B. W. Pogue, M. Testorf, T. McBride, U. L. Osterberg, and K. D. Paulsen, "Instrumentation and design of a frequency-domain diffuse optical tomography imager for breast cancer detection," *Opt. Express* **1**, 391-403 (1997).
3. S. Srinivasan, B. W. Pogue, S. Jiang, H. Dehghani, C. Kogel, S. Soho, J. J. Gibson, T. D. Tosteson, S. P. Poplack, and K. D. Paulsen, "Interpreting hemoglobin and water concentration, oxygen saturation and scattering measured in vivo by near-infrared breast tomography," *Proc. Natl. Acad. Sci. U.S.A.* **100**, 12349-12354 (2003).
4. J. C. Hebden, A. Gibson, R. M. Yusof, N. Everdell, E. M. C. Hillman, D. T. Delpy, S. R. Arridge, T. Austin, J. H. Meek, and J. S. Wyatt, "Three-dimensional optical tomography of the premature infant brain," *Phys. Med. Biol.* **42**, 4155-4166 (2002).
5. N. Ramanujam, G. Vishnoi, A. H. Hielscher, M. E. Rode, I. Forouzan and B. Chance, "Photon migration through fetal head in utero using continuous wave, near infrared spectroscopy: clinical and experimental model studies," *J. Biomed. Opt.* **5**, 173-184 (2000).

6. S. R. Arridge, "Optical tomography in medical imaging," *Inv. Problems* **5**, R41-R93 (1999).
7. N. Polydorides and H. McCann, "Electrode configurations for improved spatial resolution in electrical impedance tomography," *Meas. Sci. Technol.* **13**, 1862-1870 (2002).
8. E. E. Graves, J. Ripoll, R. Weissleder, and V. Ntziachristos, "A sub-millimeter resolution fluorescence molecular imaging system for small animal imaging," *Med. Phys.* **30**, 901-911 (2003).
9. E. E. Graves, J. P. Culver, J. Ripoll, R. Weissleder, and V. Ntziachristos, "Singular-value analysis and optimization of experimental parameters in fluorescence molecular tomography," *J. Opt. Soc. Am. A* **21**, 231-241 (2004).
10. H. Xu, H. Dehghani, B. W. Pogue, R. Springett, K. D. Paulsen and J. F. Dunn, "Near-infrared imaging in the small animal brain: optimization of fiber positions," *J. Biomed. Opt.* **8**, 102-110 (2003).
11. J. P. Culver, V. Ntziachristos, M. J. Holboke and A. G. Yodh, "Optimization of optode arrangements for diffuse optical tomography: A singular-value analysis," *App. Opt.* **26**, 701-703 (2001).
12. H. Dehghani, B. W. Pogue, S. P. Poplack and K. D. Paulsen, "Multiwavelength three dimensional near infrared tomography of the breast: Initial simulation, phantom and clinical results," *App. Opt.* **42**, 135-145 (2003).
13. H. Dehghani, B. W. Pogue, J. Shudong, B. Brooksby, and K. D. Paulsen, "Three dimensional optical tomography: Resolution in small object imaging," *App. Opt.* **42**, 3117-3128 (2003).
14. H. Dehghani, B. W. Pogue, S. Jiang, S. Poplack and K. D. Paulsen, "Optical images from Pathophysiological signals within breast tissue using three-dimensional near-infrared light," in *Optical Tomography and Spectroscopy of Tissue V*, B. Chance, R. R. Alfano, B. J. Tromberg, M. Tamura, and E. M. Sevick-Muraca, eds., *Proc. SPIE* **4955**, 191-198 (2003).
15. B. W. Pogue, S. Geimer, T. McBride, S. Jiang, U. L. Osterberg, and K. D. Paulsen, "Three-dimensional simulation of near-infrared diffusion in tissue: boundary conditions and geometry analysis for a finite element reconstruction algorithm," *Appl. Opt.* **40**, 588-600 (2001).
16. J. C. Hebden, H. Veenstra, H. H. Dehghani, E. M. C. Hillman, M. Schweiger, S. R. Arridge, and D. T. Delpy, "Three dimensional time-resolved optical tomography of a conical breast phantom," *App. Opt.* **40**, 3278-3287 (2001).
17. A. Gibson, R. M. Yusof, E. M. C. Hillman, H. Dehghani, J. Riley, N. Everdale, R. Richards, J. C. Hebden, M. Schweiger, S. R. Arridge, and D. T. Delpy, "Optical tomography of a realistic neonatal head phantom," *Appl. Opt.* **42**, 3109-3116 (2003).
18. J. P. Culver, R. Choe, M. J. Holboke, L. Zubkov, T. Durduran, A. Slemp, V. Ntziachristos, B. Chance and A. G. Yodh, "Three-dimensional diffuse optical tomography in the parallel plane transmission geometry: Evaluation of a hybrid frequency domain/continuous wave clinical system for breast imaging," *Med. Phys.* **30**, 235-247 (2003).
19. H. Jiang, K. D. Paulsen, and U. Osterberg, B. W. Pogue and Michael S. Patterson, "Optical image reconstruction using frequency domain data: simulations and experiments," *J. Opt. Soc. Am. A* **13**, 253-266 (1996).
20. M. Schweiger, S R Arridge, M Hiroaka and D T Delpy, "The finite element model for the propagation of light in scattering media: Boundary and source Conditions," *Med. Phys.* **22**, 1779-1792 (1995).
21. S. R. Arridge and M. Schweiger, "Photon-measurement density functions. Part2: Finite-element-method calculations," *App. Opt.* **34**, 8026-8037 (1995).
22. B. Brooksby, S. Jiang, C. Kogel, M. Doyley, H. Dehghani, J. B. Weaver, S. P. Poplack, B. W. Pogue, and K. D. Paulsen, "Magnetic resonance guided near infrared tomography of the breast", *Rev. Sci. Instr.* **75**, 5262-5270 (2004).
23. M. Schweiger and S. R. Arridge, "Optical tomographic reconstruction in a complex head model using a priori region boundary information," *Phys. Med. Biol.* **44**, 2703-2722 (1999).
24. H. Jiang, K. D. Paulsen, U. L. Osterberg, and M. Patterson, "Improved continuous light diffusion imaging in single and multiple target tissue-like phantoms," *Phys. Med. Biol.* **43**, 675-693 (1998).
25. Q. Zhu, N. G. Chen, and S. C. Kurtzman, "Imaging tumor angiogenesis by use of combined near-infrared diffusive light and ultrasound," *Opt. Lett.* **28**, 337 - 339 (2003).
26. M. Molinari, B. H. Blott, S. J. Cox, and G. J. Daniell, "Optimal imaging with adaptive mesh refinement in electrical impedance tomography," *Physiol. Meas.* **23**, 121-128 (2002).

1. Introduction

In the recent years, there has been a heightened interest in near-infra-red (NIR) optical tomography, for applications such as diagnostic breast cancer imaging [1-3] and for brain function assay [1, 4, 5]. In NIR tomography, the aim is to reconstruct interior optical properties of the tissue under investigation from a finite, yet incomplete set of transmission measurements taken at the tissue external boundaries. The reconstructed optical properties can give clinically useful information regarding tissue physiology and state, such as chromophore concentration and oxygen saturation. Typically, the optical source light used for excitation in

NIR studies is delivered through optical fibers and the transmitted light is also collected through the same or additional fibers which are in contact with the external surface of the tissue. Using these measurements, distributions of wavelength dependent absorption and/or scattering coefficients of the tissue are reconstructed using a model-based iterative algorithm. NIR studies have the advantage of being non-invasive, non-hazardous and can therefore be applied repeatedly to investigate functional changes in tissue over a prolonged time.

The dominance of light scattering in tissue at NIR wavelengths makes optical tomography inherently more difficult in the sense that light becomes diffuse within millimeters of travel, reducing the resolution of the reconstructed images. The image reconstruction procedure (i.e. the inverse problem) is non-linear, ill-posed and ill-conditioned [6] and to improve image reconstruction, the number of measurements are generally increased, to increase the amount of independent information. However due to experimental set-up constraints, such as the light collection strategy, source and detector fiber size and the imaging domain geometry, the total number of boundary measurements that can be taken from is often quite limited. In addition, there are constraints on the data acquisition and computation time that need to be considered for the specific application in which NIR light is used.

There have been some limited studies [7-11] on optimization of the fiber positions and measurements to get the best possible image resolution and contrast in NIR tomography. More specifically, Culver et. al [11] have showed that singular value decomposition (SVD) analysis of the weight matrix (also known as the Jacobian or sensitivity matrix) can be used to optimize detector placement in the reflectance and direct transmittance geometries of a homogeneous slab medium, and indicated that this could be extended to arbitrary geometries with heterogeneous tissue volumes. However, there remain many unknowns regarding the appropriate number of measurements required to get a sufficiently good image given the practical constraints of measurement number and image recovery algorithm, which is the subject of this paper. Furthermore, few studies have specifically investigated the effect of mesh resolution in both the forward and inverse calculations and very little is known about the quantitative increase in accuracy which is a direct result of mesh resolution and appropriate reconstruction bases. This work is an attempt to answer questions regarding the limited increase in number of measurements, more specifically benefits from the increased amount of information as well as investigating aspects that will have effects on image reconstruction procedure and resolution as well as the contrast of the reconstructed image.

In the present work, both a two dimensional (2D) circular domain and a three dimensional (3D) cylindrical geometry are investigated since most investigations to date have used either of these geometries for system and algorithm evaluation. Initially the effect of mesh resolution is investigated in the forward problem by comparing the Jacobian cross-section for various resolution 2D meshes to show improvements in numerical accuracy. Next the effect of increasing the number of measurements upon the resulting reconstructed image using singular-value analysis is investigated. Results regarding the optimized reconstruction basis are presented for the given 2D model, and the impact in the Root Mean Square (RMS) error of increased spatial sensitivity is presented as a function of increasing number of measurements. Finally a case-to-case analysis is shown by increasing the number of measurements in image reconstruction procedure and comparing the underlying image errors within the reconstructed images.

Since 3D problems have more degrees of freedom (unknown parameters), they are highly ill-determined as compared to the 2D problem. But NIR optical tomography utilizes the data from the 3D tissue volumes and therefore should be treated as a 3D imaging problem. Since light propagation in tissue is physically spread in all directions, 3D models are known to be an accurate prediction of the light fluence, whereas 2D models are simple yet inaccurate at predicting the interior fluence distributions [4, 12-17]. In order to further advance NIR optical tomography into a suitable and accurate clinical imaging modality, it is important to develop fully 3D imaging tools, yet, the major challenge in this task is to determine how to acquire large data sets which overcome the inherent limitation of the 3D problem being ill-determined

[18]. That is, to improve image reconstruction quality in 3D, the number of measurements can be increased as mentioned in 2D case, even here these measurements are quite limited.

For the chosen 3D cylindrical geometry, for example, acquiring experimental data from three different planes of fiber setup improves the reconstructed image of the entire domain as compared to one single plane of data, as there are greater numbers of measurements providing a larger set of sampling of the entire volume of interest. There are many strategies to increase measurement number and it is not clear which present the best improvement in the final image. Specifically, this work examines effects of different measurement strategies for 3D NIR tomography by presenting and quantifying the underlying effects of using a single plane of tomographic data as compared to three planes of tomographic data. Within the latter case, this work also presents, quantifies and discusses the benefits, limits and losses due to the measurement of in-plane data as compared to out-of plane data and will compare and contrast these data collection geometries from the prospective of gain and loss in the reconstructed image quality and respective computation time.

2. Methods

Conventional numerical methods for the forward calculations in NIR imaging use the Finite Element Method (FEM), which is considered as a flexible and accurate approach to modeling heterogeneous domains with arbitrary boundaries. Light transport in scattering tissue can be accurately described by the Diffusion Approximation (DA) to the Radiative Transfer Equation (RTE) [19]:

$$-\nabla \cdot \kappa(r) \nabla \Phi(r, \omega) + \left(\mu_a(r) + \frac{i\omega}{c} \right) \Phi(r, \omega) = q_0(r, \omega) \quad (1)$$

where $\Phi(r, \omega)$ is the photon density at position r and modulation frequency ω (100 MHz in this work), and $\kappa = 1/[3(\mu_a + \mu_s^{\prime})]$, the diffusion coefficient, where μ_a and μ_s^{\prime} are the probabilities per unit length of absorption and transport scattering, respectively, and $q_0(r, \omega)$ is an isotropic source term. The Robin (Type III) boundary condition is used which best describes the light interaction from a scattering medium to the external air boundary [20]. The calculated boundary data values with a frequency domain system are the amplitude and phase of the signal, from which the diffusion and absorption coefficients can be simultaneously reconstructed.

For the inverse problem, a small change in boundary data is related to a small change in optical properties through the Jacobian matrix of values. The Jacobian matrix for reconstructing both the unknowns using two different data-types is calculated using the Adjoint-method [21], and has dimensions of $(2 \times S \times D)$ by $(2 \times N)$, where S and D are the number of sources and detectors corresponding to each source respectively. N represents the number of nodes in the mesh used in the forward calculation. Here the Jacobian maps the changes in log amplitude and phase $(2 \times S \times D)$ to both absorption and diffusion changes at each node of the FEM model $(2 \times N)$. The Jacobian which maps the change in detected signal to image space has four parts:

$$J = \begin{bmatrix} J1 = \frac{\partial \ln I}{\partial \kappa}; & J2 = \frac{\partial \ln I}{\partial \mu_a} \\ J3 = \frac{\partial \theta}{\partial \kappa}; & J4 = \frac{\partial \theta}{\partial \mu_a} \end{bmatrix} \quad (2)$$

In all our analysis, only the $J2$ section is considered (dimension of $(S \times D)$ by N), which maps a small change in the absorption coefficient to a small change in measured log intensity of the signal. Since all kernels of the complete Jacobian show similar results, the discussion is limited to the results of $J2$, and shall henceforth be referred to as J .

In the reconstruction procedure presented, a modified Levenberg-Marquadt algorithm is used for calculating the estimates of μ_a , which is an iterative procedure [10] solving:

$$[\Delta\mu_a] = [\mathbf{J}^T\mathbf{J} + \lambda\mathbf{I}]^{-1} \cdot \mathbf{J}^T\mathbf{b} \quad (3)$$

Here $[\Delta\mu_a]$ is an update vector for the absorption coefficient, \mathbf{I} is the identity matrix and λ is a regularization parameter. Also, $\mathbf{b} = [\mathbf{y} - \mathcal{F}(\mu_a)]$, where \mathbf{y} is the measured (or simulated) heterogeneous boundary data and $\mathcal{F}(\mu_a)$ is the forward data for the current estimate of μ_a . In all of the presented work using simulated data, 1% noise was added to the amplitude, which is a typical noise observed in experimental data [2].

For the 2D analysis a circular model with a diameter of 86 mm centered at (0, 0) and with homogeneous optical properties of $\mu_a = 0.01 \text{ mm}^{-1}$ and $\mu_s' = 1.0 \text{ mm}^{-1}$ is considered. The light collection/delivery fibers are arranged in a circular equally spaced fashion, where one fiber is used as the source while all other fibers are used as detectors, to give 'P' number of measurements (where $P = M(M-1)$, where M is number of fibers). The source is a Gaussian source of Full Width Half Maximum (FWHM) of 3mm, and it is placed one transport scattering length within the external boundary.

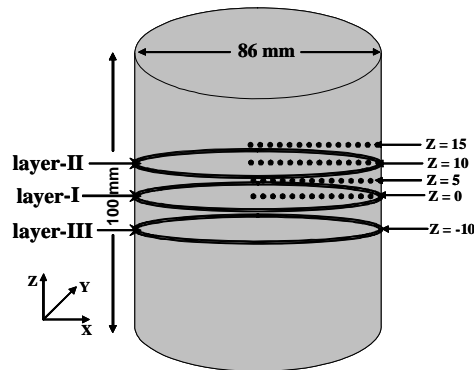


Fig. 1. Schematic diagram of data collection geometry used for the 3D cylindrical model.

For the 3D analysis, a cylindrical medium with a diameter of 86 mm having height of 100 mm centered at (0, 0, 0), with homogeneous optical properties of $\mu_a = 0.01 \text{ mm}^{-1}$ and $\mu_s' = 1 \text{ mm}^{-1}$ is used (Fig. 1). The light collection/delivery fibers are arranged in a circular and equally spaced fashion and are in either a single plane of 16 fibers or 3 planes of 16 fibers per plane, totaling 48 fibers. Specifically three different strategies for data collection are considered:

(a). Single layer data: The 16 fibers are arranged in a circular and equally spaced fashion in a single Layer-I (Fig. 1), where one fiber is used at a time as the source while all other fibers are used as detectors, to give 240 (16x15) amplitude measurements.

(b). Three layers of in-plane data: The 48 fibers are arranged in a circular equally spaced fashion in all three layers (Layers-I, II & III in Fig. 1), giving 16 fibers per plane, where one fiber is used at a time as the source while only those fibers in the same "source fiber layer" are used as detectors, to give 720 (3x16x15) amplitude measurements.

(c). Three layers of out-of-plane: Same as above, except when one fiber is used at a time as the source, all other fibers in all three planes are used as detectors. This leads to 2256 (48x47) amplitude measurements.

For the image reconstruction process, an iterative update to the Jacobian matrix was computed, after each successive image estimation. At each iteration, the objective function was evaluated to estimate the projection error. The reconstruction procedure was then stopped when the projection error decreased by less than 3%.

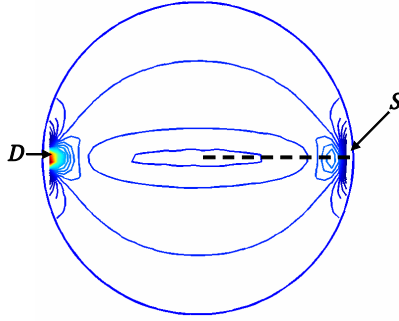


Fig. 2. The sensitivity (Jacobian) contour plot of log amplitude and μ_a for a source (S) and detector (D), which are diagonally opposite to each other as shown, calculated on a circular mesh of 9664 nodes.

2.1. 2D Mesh Resolution

In FEM the domain is divided into finite discretized sub-domains wherein the numerical accuracy and stability depends highly on this discretization (mesh resolution). Since the Jacobian represents the sensitivity of the detected signal to a small change in optical properties, the numerical accuracy of this value is crucial component of the image reconstruction problem, to study the effect of mesh resolution in 2D case, we choose different resolution meshes (with number nodes ranging from 150 to 4617 nodes) along with a high-resolution mesh of 9664 nodes for calculation of Jacobian. The Jacobian with a diagonally opposite source and detector is used, as shown in Fig. 2, from which the RMS error is calculated for each mesh with respect to the high-resolution mesh. The RMS error is calculated by interpolating the Jacobian of each mesh unto a uniformly distributed grid, allowing direct comparison of each result. Since the Jacobian represents the sensitivity of the detected signal to a small change in optical properties, the numerical accuracy of this value is a crucial component of the image reconstruction problem. Here the highest resolution mesh provides the most accurate and numerically stable solution, therefore the calculated RMS error indicates the numerical accuracy of each lower resolution mesh. The computation time taken for calculation of Jacobian and forward data is also noted as a function of mesh resolution. All the computations were carried out on Pentium-IV 2.5 GHz processor with 2 GB of RAM.

2.2. Singular-Value (SV) analysis

Singular-Value (SV) analysis for the Jacobian matrix is explained in detail elsewhere [10]. Using SV-analysis, the Jacobian is decomposed into:

$$\mathbf{J} = \mathbf{U}\mathbf{S}\mathbf{V}^T \quad (4)$$

where, \mathbf{U} & \mathbf{V} are orthonormal matrices containing the eigenvectors of \mathbf{J} and \mathbf{S} is a diagonal matrix containing the singular values of \mathbf{J} . Vectors of \mathbf{U} and \mathbf{V} correspond to the modes in the detection space and image space, respectively, while the magnitude of the singular values in \mathbf{S} represents the importance of the corresponding eigenvectors in \mathbf{U} and \mathbf{V} . More nonzero singular values indicating more modes are effective in between the two spaces, which bring more detail and improve the resolution in the space. There are normally P nonzero singular values in the diagonal matrix and these values are sorted in decreasing order. Typically only those singular values above the noise level (in this study, 1 % noise in amplitude) are used, as they contain the only useful information in the matrix. Thus, it is possible to determine whether increasing the number of measurements gives rise to an increase in the number of useful singular values, which indicates improvement in the recovered images.

In 2D, this analysis was applied to two separate cases: (1) a homogeneous case with optical properties as given before, and (2) a heterogeneous case which mimics breast optical properties [22], with properties of fibro-glandular layer being $\mu_a = 0.003 \text{ mm}^{-1}$ and $\mu_s' = 0.95 \text{ mm}^{-1}$ and having diameter of 66 mm and fatty layer surrounding it having $\mu_a = 0.006 \text{ mm}^{-1}$ and $\mu_s' = 1.1 \text{ mm}^{-1}$ with a thickness of 20mm. The number of useful singular values above the noise level were calculated as the number of measurements was increased. The mesh that was found to have an optimum resolution from the previous analysis of the Jacobian (Sec. 2.1) was used for these analysis. For both these cases, the percentage of useful measurements with respect to total number of measurements was calculated as:

$$\text{Useful measurements (in \%)} = \left[\frac{\text{Useful number of singular values}}{\text{Total number of singular values}} \right] \times 100 \quad (5)$$

Additionally, the effect of mesh resolution was studied for its impact on the number of independent boundary data points with an increase in number of measurements by calculating the rank of the Jacobian, which is defined as the maximum number of linearly independent rows/columns of a given matrix. As each row of the Jacobian indicates each measurement, the rank of the Jacobian indicates the total number of independent measurements.

Image reconstruction consists of two separate, yet equally important parts; the forward model and the inverse model. For the forward model, the mesh used in FEM needs to be such that to ensure numerical accuracy, as already discussed. For the inverse problem, however, the goal is to reduce the number of unknowns for the iterative update by the use of a reconstruction basis [23]. Therefore it is important to investigate the effects of various reconstruction basis degrees of freedom on the reconstruction. Various reconstruction basis can be used, such as second mesh basis [24], pixel basis [23] or adaptive [25, 26]. With this goal, a reconstruction basis was optimized for the given 2D problem by looking at the number of useful singular values for various pixel (reconstruction) basis. A linear pixel basis of having 100 (10 by 10) elements to 1600 (40 by 40) elements was used and the Jacobian was mapped to this basis for the analysis.

Table 1. The RMS error (with respect to the fine mesh of 9664 nodes) in the Jacobian cross-section from center to boundary, (indicated by dashed line in Fig. 2) at $y = 0 \text{ mm}$. This is tabulated as a function of mesh resolution, or number of nodes in the mesh. Last two rows show the computation time taken for calculation the Jacobian and Forward data for 16 source-detector pairs (240 measurements). For the fine mesh of 9664 nodes the computation time for Jacobian and Forward data is 98.1 sec and 28 sec respectively.

Nodes	150	425	1360	1785	2683	3047	3569	4617
RMS error	60.56	27.84	5.06	4.84	2.57	2.15	1.85	1.07
Jacobian Computation Time (in Sec.)	1.1	2.5	7.8	10.1	15.2	17.8	20.8	38.1
Forward data Computation Time (in Sec.)	0.1	0.3	0.9	1.2	1.9	2.2	2.6	9.8

2.3. Reconstruction examples

In order to understand the effect of increasing the number of measurements on total sensitivity for a given 2D model the magnitude of the Jacobian was examined as a function of number of measurements. To achieve this, the horizontal cross-section of the whole Jacobian was plotted, which was summed up over all measurements, from center to boundary, and examined as the number of measurements increased. Since the Jacobian provides relative sensitivity, a cross-section plot was normalized in each case with respect to its magnitude at the center of the model and calculated as a function of number of measurements (56 to 4032). For the 3D model, the cross-section of the total Jacobian was normalized with respect to its magnitude at the center of the model (as in the 2D case), for each case of the three different data collection strategies. Finally, for the 2D model, only the absorption coefficient was

reconstructed with an increasing number of measurements of an object with absorption inhomogeneity at various positions of domain using log of amplitude data. A circular absorption anomaly of diameter of 10 mm was used having a contrast of 2:1 compared to its background. We used the optimal forward mesh along with optimal reconstruction basis for the reconstruction procedure. A total of 2 positions of absorption inhomogeneity were considered with its center at (x,y) of $(0, 0)$, and $(30, 0)$ for various number of measurements starting from 56 to 4032.

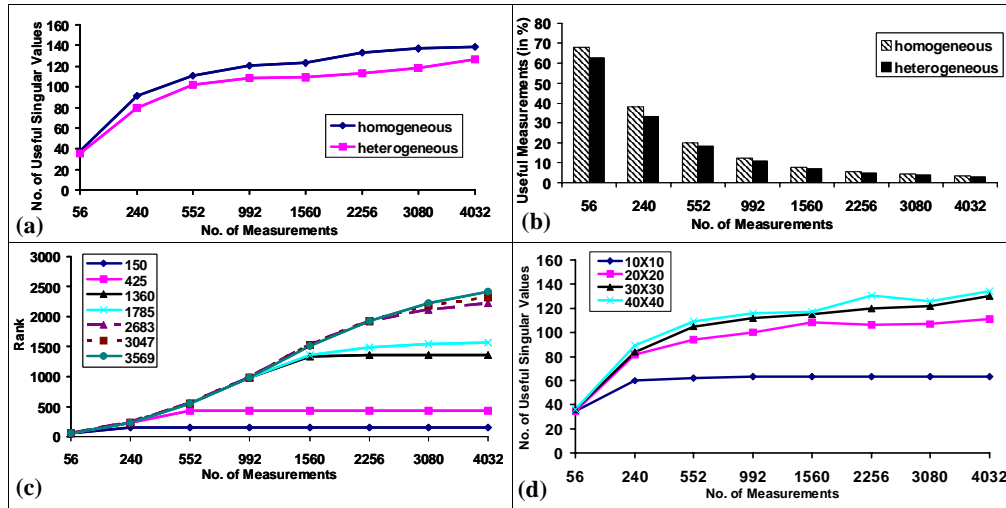


Fig. 3. Singular value analysis of homogeneous and heterogeneous 2D circular models. (a). Plot of the useful singular values versus number of measurements. (b). Plot of percentage of useful measurements versus the total number of measurements. (c). Plot of the Rank versus number of measurements is shown for a range of mesh nodes. (d). Plot of the number of useful singular values versus number of measurements is shown, for various reconstruction bases.

For the 3D case, a spherical absorption anomaly of diameter of 15 mm was assumed having a contrast of 2:1 compared to its background. A total of 3 positions of absorption inhomogeneity were considered with its center at x, y and z of $(0,0,0)$, $(30,0,0)$ and $(30,0,10)$. The anomalies were reconstructed using the noise added data (1% in amplitude) simulated from the three different fiber location strategies. Full Width at Half-Maximum (FWHM) was measured for each of the peaks in the X-Y and Z-Y planes as well as the total computation time for reconstruction process.

Table 2. The number of useful measurements above the 1% expected noise level, is shown for the 2D circular and 3D cylindrical models, having 16 source and detector fibers with one or three planes of data collection. The two upper rows have only 1 plane of collection, whereas the 2nd last row has 3 planes of collection but not between the planes, and the last row has 3 planes of data collection with complete out of plane measurements.

	Number of Unknowns	Number of Measurements	Number of Useful Singular values	Useful measurements (%)	Magnitude of largest singular value
2D	1785	240	91	37.92	796.4
3D 1layer	20163	240	107	44.58	117.1
3D 3layer in-plane	20163	720	269	37.36	164
3D 3layer out-of-plane	20163	2256	328	14.54	304.6

3 Results

Figure 2 shows a sensitivity plot of log amplitude and the absorption coefficient using a 2D mesh with 9664 nodes for a source and detector which are diagonally opposite to each other.

Table-1 shows the RMS error with respect to the high resolution mesh in the horizontal cross-section (as indicated by the dotted line in Fig. 2) using the method described earlier. The RMS error calculated here was also calculated along different cross-sections of the model and a similar trend was seen. The mesh with 1785 nodes was found to have an RMS error of less than 5% as compared to the finest mesh.

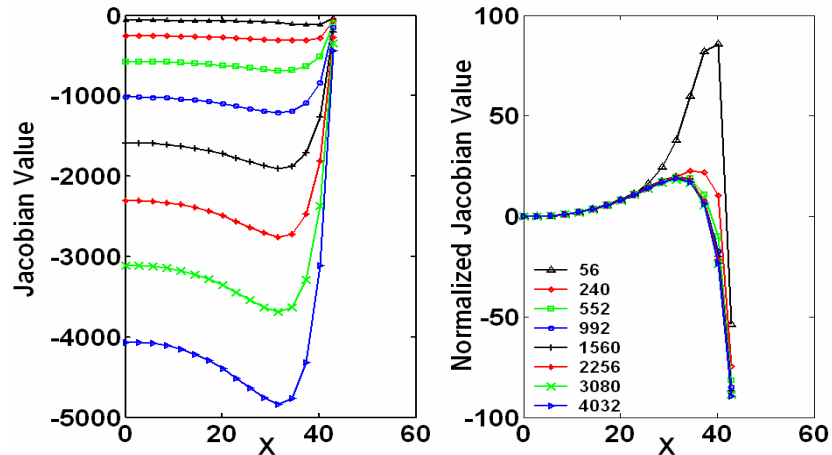


Fig. 4. Comparison of Jacobian cross-section with respect to measurement number. (a). The horizontal cross-sectional plot of the sum of 2D circular Jacobian matrix values, from center to the boundary at $y = 0$ mm. (b) The normalized sum of 2D circular Jacobian matrix values, with respect to the value at the center (at $x = 0$ mm, $y = 0$ mm). The legend gives number of measurements associated with each plot.

The 2D mesh with 1785 nodes was used for the calculation of the Jacobian and the expected noise level in the amplitude measurements was assumed to be 1%. For both the heterogeneous and homogeneous 2D cases, the number of useful singular values above the noise level were calculated, and the results are shown in Fig. 3(a). Figure 3(b) is a bar chart showing useful measurements in percentage [given by Eq. (5)] for each set of measurements. Figure 3(c) is a plot of the rank of the Jacobian versus the total number of measurements for meshes having different resolution starting from 150 to 3569 nodes versus number of measurements. The Jacobian calculated is also mapped onto a reconstruction (pixel) basis ranging from 10×10 to 40×40 . The number of useful singular values as function of pixel basis elements, for each set of measurements, are plotted in Fig. 3(d). Finally, for the 2D case, Fig. 4 shows the total sensitivity distribution at the mid-axis cross-section, as a function of the number of measurements. Table 2 shows the number of useful singular values of the 3D model Jacobian which are above the noise level (1%) for the three different strategies, and indicates the effective number of measurements which will be contributing to the reconstructed image space and quality. The number of useful singular values is higher for the three layer out-of-plane strategy. The useful percentage of measurements is higher for the 3D single plane of data, whereas the condition number is very high for the 3D three-layer out of plane case. Similar data is also included using the 2D circular geometry for comparison purposes, with 240 measurements and the same corresponding optical properties as the 3D model.

The plots of the 3D Jacobian magnitude as normalized to the value at the center of the model are shown in Fig. 5. These plots show that, all the three strategies of data collection in 3D are hypersensitive (in X & Y direction) at the boundary. Moreover this is pronounced for the 3D single-plane case. In the Z-direction (not shown) it was found that, as expected that, the sensitivity decreases as the position moves from centre to boundary for all the three cases.

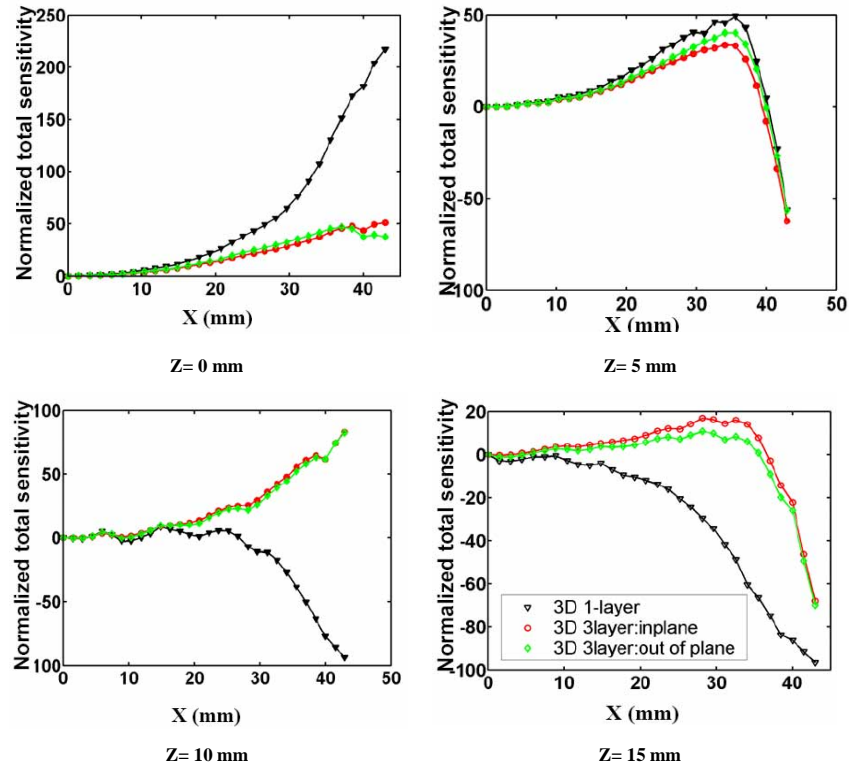


Fig. 5. The normalized cross-section in the X-Y plane, showing the total sensitivity across the dotted line in Fig. 2, from $x = 0$ mm to $x = 43$ mm (center to boundary) at $Y = 0$ mm normalized with respect to the sensitivity at the origin, (i.e. $X = 0, Y = 0$ & $Z = 0$ mm).

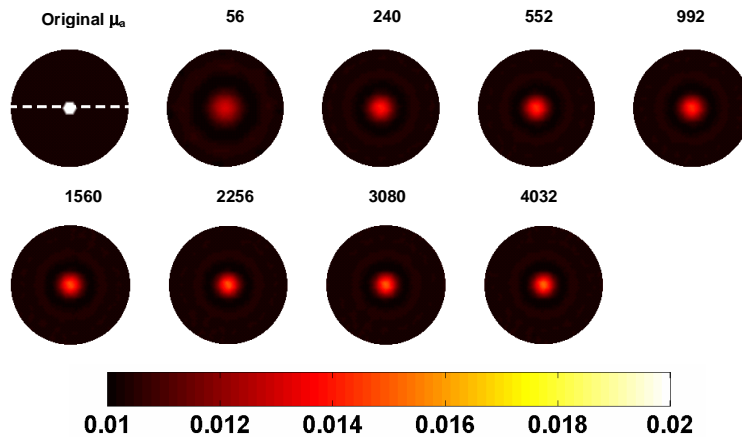


Fig. 6. The reconstruction of the μ_a distribution, using noisy simulated data of log amplitude, for a circular object with an absorbing inhomogeneity at the center. Different numbers of measurements were used as denoted above each image, ranging from 56 up to 4032 data points. The forward mesh was 1785 nodes and the pixel basis consisted of 30×30 elements. The original μ_a distribution is shown as the first image.

The 2D reconstruction of a circular object with a centralized absorption anomaly of diameter of 10mm using different number of measurements, along with original μ_a distribution, is shown in Fig. 6. The contrast of the inhomogeneity to background is 2:1 and

for these reconstructions a pixel basis of 30 x 30 elements is used, with a forward mesh consisting of 1785 nodes. Figure 7 shows the plot of logarithm of rms error in the horizontal cross-section (as shown by dotted line in Fig. 6) as a function of measurement number. The legend of the figure gives the position of the inhomogeneity (diameter of 10mm).

Table 3 summarizes the results of the 3D reconstruction. Figure 8(a) shows the reconstructed absorption coefficient distributions for a spherical absorption inhomogeneity (diameter of 15 mm) located at (0, 0, 0) with a contrast of 2:1 to background, using the data collected from the three strategies. Figure 8(b) shows the results of the same effort with a spherical inhomogeneity located near to the boundary (30, 0, 0). The results show that the quantitative values of the anomaly increases as the anomaly is moved from centre to boundary in X & Y direction. The anomaly for this location is reconstructed with 89% quantitative accuracy compared to the 15% accuracy for central location. Finally the reconstructed absorption coefficient distribution for a spherical absorption inhomogeneity (diameter - 15 mm), which is centered at (30, 0, 10) are shown in Fig. 8(c) and it can be seen that single layer case reconstructed the anomaly in the wrong location. Here, both the in-plane and out-of-plane strategies are able to give up to 84% quantitative accuracy (Table 3).

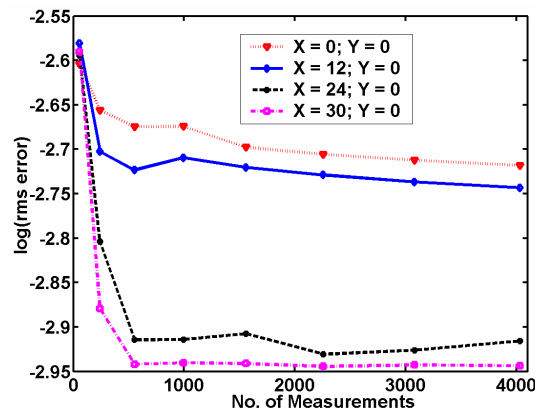


Fig. 7. A plot of logarithm of rms error in the horizontal cross-section of μ_a at $y = 0$ (as shown in original μ_a distribution of Fig. 6) versus number of measurements for various positions of an absorption inhomogeneity. These calculations used 1785 nodes in the mesh of the forward problem and a pixel basis of 30x30 elements in the reconstruction.

4 Discussion

The decrease in the RMS error for the horizontal cross-section of the 2D Jacobian for a given source-detector (diagonally opposite each other) for a mesh greater than 1500 nodes as compared to 9664 nodes (Table-1) is below 5%. It should be noted that the other kernels of the Jacobian, for example $J_3 \left(\frac{\partial \theta}{\partial \kappa} \right)$, showed better accuracy (2%) when the mesh had 1785

nodes or greater. As with many iterative reconstruction problems, optical tomography requires repeated forward calculations and re-computation of the Jacobian, thereby increasing mesh resolution which further implies increase in computational time, which is clearly evident from last two rows of Table 1. A computation limit of 10 seconds per iteration, lead to a choice of mesh resolution with 1785 nodes for the forward problem in two-dimensional case, and extending this same level of resolution to 3D would require nearly 80,000 nodes, which is near the limit of what can be done computationally. Thus much of the 2D study presented here was run at the level of 1785 nodes. Since the computation of the Jacobian using the FEM relies on the discretization of the domain and the accuracy of the numerical model depends on

Table 3. The computation time and accuracy of the 3D reconstruction is shown for the three different data collection strategies, along with three different locations of the anomaly for each.

Strategy	Position of anomaly (original)	Iterations	Total Computation time (s)	Quantitative accuracy (%) of the reconstructed anomaly	FWHM along X-axis (mm)	FWHM along Z-axis (mm)
3D: 1layer	(0,0,0)	11	3179	15%	16.1	25.2
	(30,0,0)	14	4046	89%	17.2	23.3
	(30,0,10)	10	2890	-	-	-
3D 3layer in-plane	(0,0,0)	14	8022	14%	16.5	25.3
	(30,0,0)	14	8022	80%	13.1	18.7
	(30,0,10)	12	6876	110%	11.2	18.6
3D 3layer out-of-plane	(0,0,0)	6	10926	11%	23.7	24.1
	(30,0,0)	9	16389	78%	13.6	18.9
	(30,0,10)	8	14568	84%	13.2	18.7

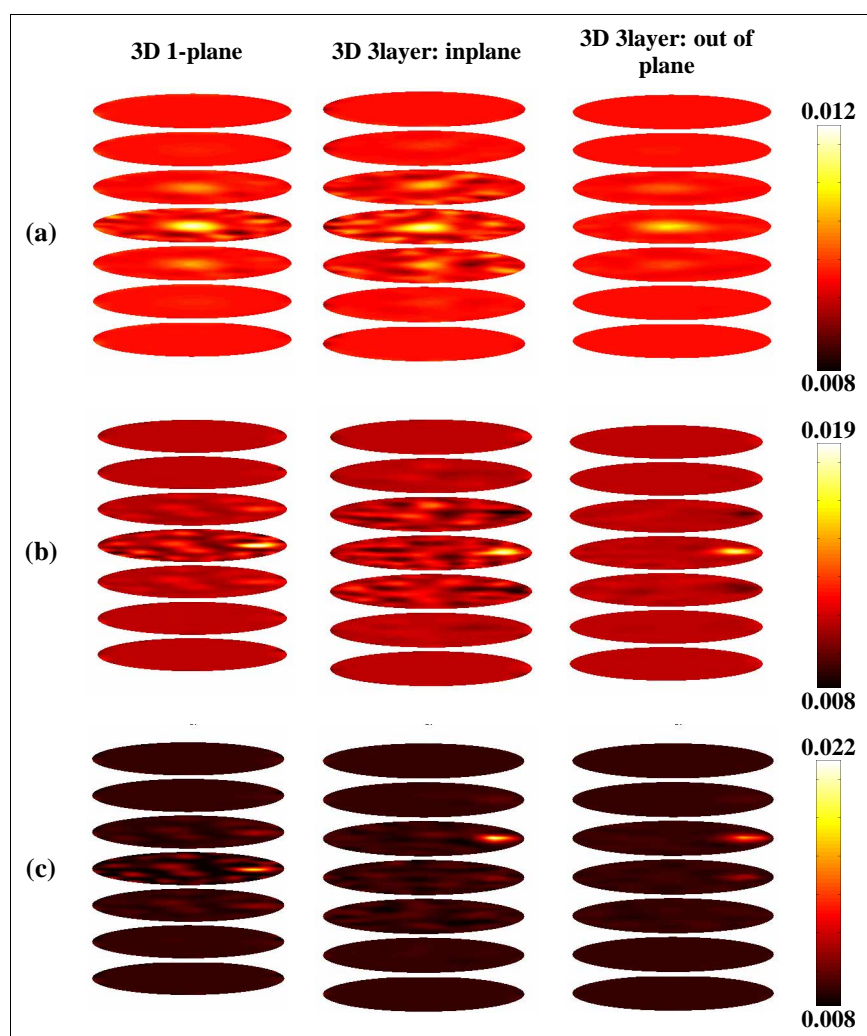


Fig. 8. The reconstructed absorption coefficient distribution for the cylindrical object with a spherical absorption inhomogeneity (diameter of 15mm and contrast 2:1 with respect to background) located at x, y and z locations (a) (0,0,0), (b) (30,0,0) and (c) (30,0,10). The three columns of images show the results achieved with the three different data collection schemes.

this discretization and the associated integration of the shape functions, the resolution of the mesh and the associated optical properties will affect these results. For example, if the absorption coefficient is much smaller, then lower resolution meshes may be adequate, as the problem becomes more energy conserving, whereas for a higher absorption or scattering problem, a higher resolution mesh will be needed to ensure numerical accuracy within each FEM element for a lossy problem. Note also that for spectral reconstruction [3] with six wavelengths data, each iteration takes about 30 sec for 1785 nodes mesh.

For a heterogeneous or homogeneous 2D case, number of useful singular values, which are above the noise level (1% in amplitude) showed similar trends and behavior with increasing numbers of measurements, as evident from Fig. 3(a). Further, the percentage of useful measurements (useful singular values) drops exponentially as the number of measurements is increased, Fig. 3(b). It is worth noting that for a heterogeneous model, since light propagation becomes more complex, and in this case more diffusive, the total number of useful measurements is slightly lower than that of homogeneous model. In this work, useful singular values are defined as the ones which are above noise level (1%). This is used only for optimizing the parameters used in the reconstruction procedure, but in the actual reconstruction procedure, regularization is used to reduce the condition number.

Next, the effect of the 2D mesh resolution was investigated, for its impact upon the number of independent available measurements. From Fig. 3(c), it is evident that if the degrees of freedom (mesh resolution) in the forward problem is less than the total number of measurements, then increasing the number of measurements does not increase the number of independent measurements (i.e. the rank), since the rank is predominantly restricted by the number of nodes in the mesh. For example, given a system from which only 240 measurements are available, any mesh which has a resolution of 240 nodes or more will give the same number of independent measurements. Therefore no additional measurements can be gained in terms of independent information by increasing the mesh resolution. Given a 2D mesh of 1785 nodes, for example, no considerable gain in independent data can be obtained when the number of measurements are increased above 1560 (40 source and detectors). At this point, it will be worth remembering that, in real time there is a physical constraint on number of measurements, because of the physical geometry and fiber size. To take an example, for a circular test phantom of 86 mm diameter and fiber of 6 mm diameter, no more than 40 fibers (which corresponds to 1560 measurements) can be arranged around the outer boundary of domain. However this issue becomes more important perhaps for non-contact imaging systems in which the number of source-detector locations can be arbitrarily large.

Using a 2D mesh of 1785 nodes, the effect of an increase in the reconstruction (regular pixel) basis resolution upon reconstruction was investigated [Fig. 3(d)]. An increase in pixel basis elements increases the number of useful singular values, but there is no significant improvement in the pixel basis from 30×30 (900 elements) to 40×40 (1600 elements). This is very interesting, since one would assume that fewer degrees of freedom for the inverse problem would produce a better solution. But although the problem may become better posed, the rank will be similar to that shown in Fig. 3(d). However, these results indicate the best possible resolution obtainable is by using the 40×40 pixel basis and again these results will be dependent on the physical problem dimension and level of complexity. Figure 4 shows that increasing the number of measurements for a 2D model increases the sensitivity of the problem, as evident from magnitude plot of the Jacobian (calculated from 1785 nodes mesh). Also shown in Fig. 4 is a normalized plot, relative to the central value, and indicates that for fewer number of measurements, the sensitivity is maximal near the boundary and lower at the center, as expected. By increasing the number of measurements, eventually the hypersensitivity near to the boundary reduced and the sensitivity became uniform regardless of distance from boundary. Finally, it is observed that increasing the number of measurements above 552 (24 sources and detectors) did not result in any further improvement in the sensitivity distribution.

For the 3D model, Table 2 shows that three layers of out-of-plane measurements yields a higher number of useful singular values, but the useful percentage of the total measurements

was below 15%. An increase in number of measurements means more data acquisition time and more computation time. Non-linear iterative image reconstruction procedures in NIR imaging use repeated calculation of the forward data. Therefore increasing the number of sources and measurements substantially increases the computation time. In comparing the three layer in-plane and three layer out-of-plane data collection strategies, having more than three times the measurements in the latter case improves the number of useful singular values only by 22%. The improvement in the number of useful singular values is not significant if the data acquisition time is considered as well as the computation time. The magnitude of the singular values indicates the importance of that eigenvector in the image space, which is directly related to reconstructed image contrast that can be achieved. To compare the magnitude of the largest singular value, even though it is at its highest for the three layer out-of-plane strategy, it should be noted that only 3 of the singular values are above 164 (magnitude of largest singular value of 3D 3layer-in-plane), indicating that there would not be dramatic differences in the reconstructed image contrast in both these cases. If the magnitude of largest singular value in 2D and 3D are compared, in 2D the magnitude is higher, whereas the number of useful singular values are lower than 3D, indicating that the modes that contribute to image space are fewer and the quality of the reconstructed image in 2D will be lower than 3D. Even though magnitude of the singular values dictate the contrast, the singular vectors associated with it will tend to affect the reconstructed image quality. The magnitude of the largest singular value in the 3D 3layer cases are the same because of the smoothness of the singular vectors in the case of 3D 3 layer: out-of-plane, the reconstructed image quality is better than the rest cases (Fig. 8). The FWHM analysis also confirms this.

It should be noted that there is always a trade-off between image quality and computation time. Therefore having out-of-plane data increases the image resolution, but taking into consideration the overall computation time, this improvement is perhaps not so significant. The computation time per iteration is high in the case of out-of-plane data (computation time per iteration: 2D problem – 70 sec; single-layer – 289 sec; three layer: in-plane – 573 sec; three layer: out-of-plane – 1821 sec).

Figure 5 indicates that for the 3D model with a single measurement plane case, the total sensitivity is higher near the boundary, as compared to the three plane data case and by increasing the number of measurements the sensitivity near the boundary is decreased. The results show that although the sensitivity is still higher at the boundary with three planes of data acquired, there is no significant difference in the sensitivity pattern observed between three layer in-plane or out-of-plane strategies.

Since only one component of the full Jacobian matrix, J_2 in Eq. (2), has been examined here, images have also been reconstructed for μ_a using log amplitude data for a 2D forward mesh of 1785 nodes and a reconstruction basis 30 by 30 pixel basis. Noisy simulated data were generated for various radial positions of the absorption inhomogeneity with a contrast of 2, relative to the background and having a diameter of 10 mm. The log of RMS error was calculated as the difference in the original and the reconstructed horizontal cross-sections of each image (Fig. 6) as a function of number of measurements and these were plotted in Fig. 7. The results show that, as evident from Fig. 7, although there is a decrease in the RMS error as the number of measurements is increased, the improvement in the reconstructed images is not significant for measurements greater than 552 (corresponding to 24 fibers). However, for a central anomaly, the RMS error continued to decrease with increasing number of measurements, whereas for an anomaly near the boundary the RMS error does not improve more than 0.5% with respect to 552 measurements.

To study the effect of data collection strategies on the 3D reconstructed image, the FWHM (Full Width at Half Maximum) of the peaks for all the reconstructed cases have been calculated and compared, Table 3. As the inhomogeneity moves from the centre towards the boundary, the FWHM reduces for both of the three layer cases and it remains approximately the same for the single layer case. For example, when the inhomogeneity is placed at (30,0,0), Fig. 8(b), the FWHM (in the X-cross section) values for single layer is 17.2mm and for the three-layers in-plane and out-of-plane strategies is 13.1mm and 13.6mm respectively. It is

evident from the reconstruction examples that the quantitative values of the inhomogeneities increase as the object moves from the centre to boundary, which is in close match with Jacobian analysis above. Reconstruction of absorption using single layer data, is not accurate, in a case where the anomaly is not presented in the imaging plane, such a case results are presented in Fig. 8(c). In this case, single-layer reconstructed image shows the inhomogeneity at a false position (reconstructed: (30,0,0); actual: (30,0,10)). Most of the 3D NIR studies indicate that, the quantitative accuracy of the images will be poor due the partial volume effect in three dimensions[13,16,17] and these quantification can be greatly improved by the use of more sophisticated regularization and the addition of penalty terms into Eq. (3).

5 Conclusions

In this investigation, the mesh resolution and numerical accuracy in the 2D and 3D forward problems were examined, using specific data-collection geometries. Several choices such as domain size, optical properties and anomaly position and size were kept fixed, relative to typical breast cancer imaging situations. It was shown that increasing the number of measurements increases the total amount of information available, and these specifically enhance the recovery of the central region of the model, regardless of dimensionality. Further, by increasing the number of measurements, the rank of the problem (i.e. amount of independent useful information) may not increase if the degrees of freedom (i.e. number of nodes in the mesh) are low. Reconstruction basis plays an important role in the inverse problem and it has been found that a pixel basis of 30×30 is optimal for a typical breast imaging problem.

More specifically for a 3D imaging problem, this work has shown the benefits and drawbacks of multi-plane data collection as well as the use of in-plane versus out-of-plane data measurements strategies. It has been shown that the use of single-plane of data in a 3D model is perhaps adequate, in terms of image quality, computation time and data collection time, if the anomaly being imaged is within the plane of measurements. However, if prior information such as plane of interest is not known, it has been shown that multi-plane data is crucial. The use of in-plane and out-of-plane data has been addressed and is shown that although the use of out-of-plane data provides more independent and useful information for image reconstruction, the magnitude of this additional information does not provide enough advantages worth the data acquisition and image computation time.

Finally it is worth noting that the 3D study has been limited to 16 source/detection fibers per plane. The addition of more measurement fibers and/or investigation of a different image reconstruction basis, such as those performed for the 2D problem can be easily extended for the presented 3D problem. The technique and analysis described here can be used as a tool to improve resolution and contrast, given prior information about the domain being imaged. This specific study was undertaken to better understand the parameters and capabilities of existing breast imaging system at Dartmouth and to focus on software improvements which may increase its recovery of lesion information.

Acknowledgments

P.K.Y. acknowledges support from the US DOD for Breast Cancer predoctoral fellowship (BC050309). As well, this work has been sponsored by the National Cancer Institute through grants RO1CA69544, PO1CA80139, and the DOD through DAMD17-03-1-0405.